The Astronomical Journal, 171:334 (16pp), 2026 June https://doi.org/10.3847/1538-3881/ae5b6d

Investigation of Transit Timing and an Optical Transmission Spectrum of the Hot Jupiter WASP-11 b

Napaporn A-thano[1], Supachai Awiphan[1], Eamonn Kerins[2], Akshay Priyadarshi[2], Iain McDonald[2,3], Orarik Tasuya[1], Ronnakrit Rattanamala[4], Ing-Guey Jiang[5], Yogesh C. Joshi[6], Fan Yang[7], Ida Janiak[2], Patcharawee Munsaket[8], Yasir Abdul Qadir[9], Smanchan Chandaiam[1], Boonyarit Choonhakit[1], Suwanit Wutsang[1], Boonrucksar Soonthornthum[1], and Vik S Dhillon[10,11]

[1] National Astronomical Research Institute of Thailand, 260 Moo 4, Donkaew, Mae Rim, Chiang Mai, 50180, Thailand; napaporn@narit.or.th, supachai@narit.or.th
[2] Jodrell Bank Centre for Astrophysics, University of Manchester, Oxford Road, Manchester, M13 9PL, UK
[3] Department of Physical Sciences, The Open University, Walton Hall, Milton Keynes, MK7 6AA, UK
[4] Department of Physics and General Science, Faculty of Science and Technology, Nakhon Ratchasima Rajabhat University, Nakhon Ratchasima, 30000, Thailand
[5] Department of Physics and Institute of Astronomy, National Tsing-Hua University, Hsinchu 30013, Taiwan
[6] Aryabhatta Research Institute of Observational Sciences (ARIES), Manora Peak, Nainital 263001, India
[7] Département d'Astrophysique/AIM, CEA/IRFU, CNRS/INSU, Univ. Paris-Saclay, Univ. de Paris, 91191, Gif-sur-Yvette, France
[8] School of Physics, Institute of Science, Suranaree University of Technology, 111 University Avenue, Suranaree, Nakhon Ratchasima 30000, Thailand
[9] Department of Physics and Astronomy, FI-20014 University of Turku, Finland
[10] Department of Physics and Astronomy, University of Sheffield, Sheffield, S3 7RH, UK
[11] Instituto de Astrofísica de Canarias, E-38205 La Laguna, Tenerife, Spain
Received 2025 September 29; revised 2026 April 1; accepted 2026 April 1; published 2026 May 8

Abstract

WASP-11 b/HAT-P-10 b is an inflated hot Jupiter, which has a low density that makes it a good target for atmospheric studies using the transmission spectroscopy technique. In this work, we present 31 new transit light curves of WASP-11 b/HAT-P-10 b, obtained through the Spectroscopy and Photometry of Exoplanet Atmospheres Research Network. These data were analyzed along with previously published ground-based observations and space-based data from TESS. We refine the planetary parameters of WASP-11 b/HAT-P-10 b and perform a transit timing analysis using data spanning 16 yr. The updated ($O - C$) diagram shows no significant evidence of orbital decay. Transit-timing variation analysis reveals no significant signals indicative of additional planets. Atmospheric analysis using multiband optical observations indicates a strong Rayleigh scattering slope in the transmission spectra, which may originate from the planetary atmosphere itself or be influenced by contamination such as stellar activity or light from the companion star.

Unified Astronomy Thesaurus concepts: Transit photometry (1709); Transmission spectroscopy (2133); Exoplanet atmospheres (487); Exoplanets (498); Exoplanet dynamics (490); Transit timing variation method (1710)

Materials only available in the online version of record: machine-readable tables

1. Introduction

In 2009, the transiting exoplanet WASP-11 b/HAT-P-10 b was independently discovered by two ground-based surveys: the Wide-Angle Search for Planets (WASP; R. G. West et al. 2009) and the Hungarian-made Automated Telescope Network (HATNet; G. Á. Bakos et al. 2009). The planet orbits an early K-dwarf star, WASP-11A/HAT-P-10A ($V = 12$, distance $= 129.88 \pm 0.98$ pc; based on a Gaia DR3 parallax of 7.6997 ± 0.0579 mas), with a period of 3.722 days. G. Á. Bakos et al. (2009) reported the discovery using the HAT-10 telescope as part of the HATNet survey and derived a planetary mass of $0.46 \pm 0.03\ M_{\rm Jup}$, a radius of $1.05^{+0.05}_{-0.03}\ R_{\rm Jup}$, and a mean density of 0.498 ± 0.064 g cm^{-3}. The planet is primarily composed of hydrogen and helium, with an equilibrium temperature of $T_{\rm eq} = 1030^{+26}_{-19}$ K. R. G. West et al. (2009) also confirmed the discovery with SuperWASP-North and reported slightly different parameters: $M_{\rm p} = 0.53 \pm 0.07\ M_{\rm Jup}$, $R_{\rm p} = 0.91^{+0.06}_{-0.03}\ R_{\rm Jup}$, and $T_{\rm eq} = 960 \pm 70$ K. Follow-up radial velocity monitoring and adaptive optics imaging by H. A. Knutson et al. (2014) and H. Ngo et al. (2015) revealed a low-mass stellar companion. The Global Architecture of Planetary Systems (GAPS) program (L. Mancini et al. 2015) measured the Rossiter–McLaughlin effect, indicating a well-aligned spin–orbit configuration.

Transit-timing variations (TTVs) of WASP-11 b/HAT-P-10 b were first investigated by X.-b. Wang et al. (2014) through an ($O - C$) analysis. They reported a constant orbital period and found no evidence of a significant TTV signal. They also considered the possibility of an outer companion via the light-travel time effect (J. B. Irwin 1952). L. Mancini et al. (2015) combined data from the GAPS program with the Exoplanet Transit Database (ETD) and suggested that the underestimated timing uncertainties might be due to either an unseen planetary companion or stellar activity. However, their Lomb–Scargle periodogram analysis did not reveal any significant signal, ruling out the hypothesis. Following the launch of the Transiting Exoplanet Survey Satellite (TESS; G. R. Ricker et al. 2014), observations of WASP-11 b/HAT-P-10 b began in 2021. TESS data have since been analyzed in combination with published transit timings to refine the system ephemeris, investigate orbital variations, and search for TTVs (E. S. Ivshina & J. N. Winn 2022; G. Maciejewski et al. 2023;

H. Er et al. 2024). S. Yalçınkaya et al. (2024) incorporated their own transit observations together with ETD data and one TESS sector. Their analysis showed no significant periodic changes in the TTV diagram and yielded an orbital decay rate of $dP/dE = -9.6 \pm 5.98 \times 10^{-10}$ day cycle^{-1}, corresponding to a stellar tidal quality factor of $Q'_\star > 4.1 \times 10^2$. In contrast, W. Wang et al. (2024) analyzed three TESS sectors combined with literature midtransit times to test for long-term orbital variations using a leave-one-out cross-validation (LOOCV) approach, and reported an increasing period derivative of $\dot{P} = 23.32 \pm 6.69$ ms yr^{-1}.

The study of transiting exoplanets provides not only constraints on TTVs but also valuable insights into planetary atmospheres (S. Awiphan et al. 2016; L. Bai et al. 2022; B. Edwards et al. 2023). TTV analysis is an effective method for detecting additional planets and characterizing the orbital evolution of planetary systems (E. Agol et al. 2005). Additionally, multiwavelength observations acquired during transit events enable the measurement of the planetary radius at different wavelengths, providing a vital baseline for future atmospheric analyses and transmission spectroscopy (S. Seager & D. D. Sasselov 2000). In this work, we observed transit events of WASP-11 b/HAT-P-10 b through multiband photometry as part of the Spectroscopy and Photometry of Exoplanet Atmospheres Research Network (SPEARNET), a long-term program aimed at characterizing the atmospheres of hot transiting exoplanets using transmission spectroscopy (N. A-thano et al. 2023; J. J. C. Hayes et al. 2024). This approach enables the simultaneous investigation of TTVs and atmospheric properties via broadband transmission spectroscopy. Together, these diagnostics provide key constraints on the formation and evolution of planetary systems.

Since 2016, SPEARNET has conducted multiband photometric follow-up observations of WASP-11 b/HAT-P-10 b to study its transit events, TTVs, and transmission spectrum. In this paper, we present new ground-based multiband photometric observations of 31 transits of WASP-11 b/HAT-P-10 b. These data are combined with previously published light curves and TESS observations to refine the planetary parameters, investigate TTVs, and constrain the optical transmission spectrum of this hot Jupiter. The structure of the paper is as follows: Section 2 describes the observational data and sources. Section 3 presents the light-curve analysis. Section 4 examines the TTVs, while Section 5 discusses the optical transmission spectrum. Finally, conclusions and discussion are given in Section 6.

2. Observational Data

2.1. SPEARNET Ground-based Observations and Data Reduction

From 2016 to 2024, we conducted multiband photometric observations of WASP-11 b/HAT-P-10 b using the SPEARNET telescope network. These observations were obtained with several facilities, including the 2.4 m and 1 m Thai National Telescopes (TNT) at the Thai National Observatory (TNO) in Thailand, the 0.7 m Thai Robotic Telescope at Gao Mei Gu Observatory (TRT-GAO) in China, the 0.7 m Thai Robotic Telescope at Sierra Remote Observatories (TRT-SRO) in the USA, and the 0.7 m Regional Observatory for the Public in Nakhon Ratchasima (ROP-NM) and Chachoengsao (ROP-CC), Thailand. Instrument specifications are provided in Table 1. Notably, the observation obtained on 2016 December 22 at TRT-GAO was graciously conducted remotely by Her Royal Highness Princess Maha Chakri Sirindhorn during her visit to the Thai National Observatory (Figure 1). In total, we obtained 31 transit light curves, comprising 21 full and 10 partial transits, as summarized in Table 2.

The CCD data reduction was performed using standard tasks in IRAF[12] (D. Tody 1986, 1993). Astrometric calibration of the science images was carried out with Astrometry.net (D. Lang et al. 2010), and aperture photometry was performed using Source Extractor (E. Bertin & S. Arnouts 1996). Reference stars were selected from nearby stars within 3 mag of WASP-11/HAT-P-10 that showed no brightness variations. A 5σ clipping method was applied to remove outlier points from the light curves. Differential light curves were constructed by dividing the flux of WASP-11/HAT-P-10 by the sum of the fluxes of the selected reference stars. All time stamps were converted to Barycentric Julian Date in Barycentric Dynamical Time (BJD_{TDB}) using barycorrpy (S. Kanodia & J. Wright 2018). The normalized light curves are provided in machine-readable format in Table A1.

2.2. Literature Ground-based Data

In addition to the transit light curves of WASP-11 b/HAT-P-10 b obtained from our observations, we used 10 publicly available light curves from previous studies. These include one i'-band and one z'-band light curve from the KeplerCam CCD on the FLWO 1.2 m telescope provided by G. Á. Bakos et al. (2009). Three light curves from the GAPS program (L. Mancini et al. 2015) were also included: one Gunn-r filter light curve observed with the Cassini 1.52 m telescope, one Cousins-I filter light curve from the Zeiss 1.23 m telescope, and one Cousins-R filter light curve from the IAC 80 cm telescope. Additionally, three transit light curves from G. Maciejewski et al. (2023) were incorporated, including one *clear* filter light curve obtained with the PIW 0.6 m Cassegrain telescope and two Cousins-R light curves observed with the 1.2 m Cassegrain telescope and the 0.9 m Ritchey-Chrétien telescope, respectively. Finally, two R-band light curves obtained with the 1 m telescope at TÜBITAK National Observatory from S. Yalçınkaya et al. (2024) were included.

2.3. TESS Data

WASP-11 b/HAT-P-10 b was observed by TESS in three sectors between 2021 and 2024, under the TESS Input Catalog ID TIC 85593751. Four transit light curves were obtained in Sector 42 from 2021 August 23 to September 10, seven light curves in Sector 58 from 2022 November 1 to 23, and five light curves in Sector 85 from 2024 October 31 to November 18. The TESS light curves were downloaded from the Mikulski Archive for Space Telescopes (MAST).[13] We used the Pre-Search Data Conditioning light curves, which are calibrated by the Science Processing Operations Center pipeline (J. M. Jenkins et al. 2016). The TESS time stamps

[12] IRAF is distributed by the National Optical Astronomy Observatories, which are operated by the Association of Universities for Research in Astronomy, Inc., under a cooperative agreement with the National Science Foundation (http://iraf.noao.edu/).
[13] https://archive.stsci.edu/

Table 1
The Instrumental Specifications of the SPEARNET Network Facilities Used in This Work

Telescope	CCD Camera	CCD Pixel Size (pixels)	Field Of View (arcmin^2)	Number of Transits
2.4 m TNT	ULTRASPEC[a]	1024 × 1024	7.68 × 7.68	11 full, 2 partial
1 m TNT	Andor iKon-M 934	1024 × 1024	23.4 × 23.4	1 full, 1 partial
0.7 m TRT-GAO	Andor iKon-L 936	2048 × 2048	20.9 × 20.9	2 full, 1 partial
0.7 m TRT-SRO	Andor iKon-M 934	1024 × 1024	20.9 × 20.9	4 full, 3 partial
0.7 m ROP-NM	ProLine PL16803 Monochrome	4096 × 4096	28 × 28	2 full, 1 partial
0.7 m ROP-CC	ProLine PL16803 Monochrome	4096 × 4096	28 × 28	1 full, 2 partial

Note.
[a] ULTRASPEC is a high-speed frame-transfer EMCCD camera developed by V. S. Dhillon et al. (2014).

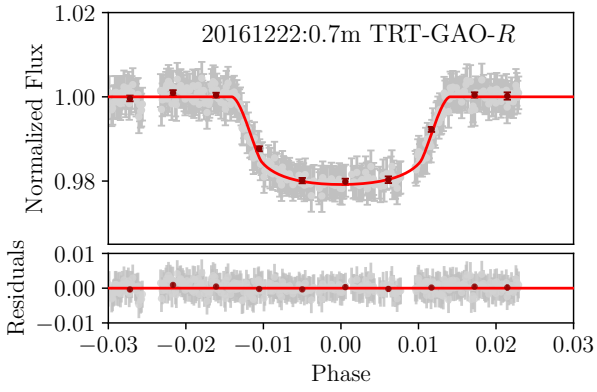

Figure 1. The normalized transit light curve of WASP-11 b/HAT-P-10 b was obtained with the 0.7 m TRT-GAO telescope in the *R* filter on 2016 December 22, during an observation graciously conducted remotely by Her Royal Highness Princess Maha Chakri Sirindhorn while visiting the Thai National Observatory. The best-fit model from `TransitFit` is shown as a solid line, and the residuals after model subtraction are displayed in the lower panel.

were converted from Barycentric `TESS` Julian Date to Barycentric Julian Date (BJD_{TDB}) by adding 2,457,000.

3. Light-curve Modeling

To derive the planetary parameters of WASP-11 b/HAT-P-10 b, we employed `TransitFit`, a Python package designed for the simultaneous fitting of multi-filter and multiepoch exoplanet transit observations (J. J. C. Hayes et al. 2024). This package utilizes the `batman` transit model (L. Kreidberg 2015) and the `dynesty` dynamic nested sampling routines (J. S. Speagle 2020) to estimate system parameters. The transit light curves were divided into two groups: ground-based and `TESS`. For both datasets, each individual light curve was detrended using a second-order polynomial model. This detrending was performed simultaneously with the transit light-curve fitting within `TransitFit`.

In the initial stage of the `TransitFit` retrieval, we adopted the host star's effective temperature, $T_{\rm eff} = 4800 \pm 100$ K, and surface gravity, $\log g = 4.52 \pm 0.1$, as reported in the Gaia EDR3 catalog.[14] The metallicity, $[{\rm Fe/H}] = 0.120 \pm 0.09$ dex, was adopted from A. S. Bonomo et al. (2017), and a circular orbit was assumed for WASP-11 b/HAT-P-10 b. Initial values for the orbital period P, epoch of midtransit T_0 (BJD), orbital inclination i (deg), semimajor axis a (in units of stellar radius, R_*), and planetary radius R_p (in units of R_*) for each filter are listed in Table 3.

We first determined the best-fit orbital period, P, for the ground-based and `TESS` datasets. A Gaussian distribution of 3.722 479 ± 0.000 001 days was used to obtain the optimal value. The orbital inclination, i (deg), and semimajor axis, a (in units of stellar radius, R_*), were allowed to vary during the fitting. The best-fit values for each dataset are presented in Table 4. Final values were calculated by combining the results from both datasets using a weighted mean. We find that WASP-11 b/HAT-P-10 b has an orbital period of $3.7224797 \pm 7 \times 10^{-8}$ days, an inclination of $i = 88.28 \pm 0.06$ degrees, and a star–planet separation of $a/R_* = 12.17 \pm 0.04$. These results are consistent with previous studies within 1σ.

Next, we investigated the TTVs using the `allow_TTV` function in `TransitFit`. The final values of the orbital period, inclination, and semimajor axis were held fixed, while the midtransit time (t_m) for each transit, the planetary radius (R_p/R_*), and the limb-darkening coefficients (LDCs) for each filter were allowed to vary. The derived midtransit times (t_m) and corresponding epochs (E) are listed in Table B1, while the values of R_p/R_* for each filter are presented in Table 5.

The LDCs for each filter were calculated using the `Coupled` fitting mode in `TransitFit`, adopting a quadratic limb-darkening model. This calculation employed the Limb Darkening Toolkit (LDTk; T. O. Husser et al. 2013; H. Parviainen & S. Aigrain 2015) together with the host star's properties ($T_{\rm eff}$, metallicity [Fe/H], and $\log g$). The derived LDCs for each filter from the `Coupled` fitting mode are presented in Table 5.

The normalized light curves of WASP-11 b/HAT-P-10 b observed with the 2.4 m telescope and `TESS`, together with their best-fit transit models and residuals, are shown in Figures 2 and 3. Individual fits for the 18 light curves, obtained from the TRT-GAO, TRT-SRO, ROP-CC, ROP-NM, and 1 m TNT telescopes, are presented in Figure C1.

4. Transit-timing Analysis

4.1. Updated Linear Ephemeris

By combining a long baseline of observed transit events, we used midtransit times derived with `TransitFit` from a total of 50 events (listed in Table B1) for the timing analysis. First, a linear ephemeris model was applied, assuming a circular orbit with a constant orbital period. The updated linear

[14] Gaia archive: https://archives.esac.esa.int/gaia.

Table 2
The Details of WASP-11 b/HAT-P-10 b Transit Observations Obtained with the SPEARNET Telescopes

Observation Date	Epoch[a]	Telescope	Filter	Exposure Time (s)	Number of Images	Total Duration of Observation (hr)	PNR (%)[b]	Transit Coverage
2016 Dec 7	394	0.7 m ROP-CC	V	60	218	4.74	0.37	Egress only
		0.7 m ROP-NM	R	30	278	3.43	0.18	Full
2016 Dec 22	398	0.7 m ROP-NM	R	30	257	4.52	0.13	Egress only
		0.7 m TRT-GAO	R	30	356	5.16	0.12	Full
2017 Jan 17	405	0.7 m TRT-GAO	R	30	239	3.19	0.18	Ingress only
2017 Nov 22	488	0.7 m ROP-CC	V	60	111	2.74	0.22	Egress only
		0.7 m ROP-NM	R	30	188	4.60	0.24	Full
2017 Dec 18	495	2.4 m TNT	i'	3.56	4316	4.78	0.11	Full
2018 Jan 2	499	2.4 m TNT	g'	2.43	5581	4.43	0.08	Full
2018 Nov 3	581	2.4 m TNT	r'	1.95	9044	5.10	0.08	Full
2018 Nov 18	585	2.4 m TNT	g'	3.57	4868	5.05	0.07	Full
2018 Dec 3	589	0.7 m ROP-CC	V	60	126	4.62	0.18	Full
2020 Dec 9	787	0.7 m TRT-GAO	I	40	184	4.77	0.15	Full
		2.4 m TNT	z'	12.78	1704	6.46	0.10	Full
2021 Nov 24	798	2.4 m TNT	r'	5.12	1137	1.98	0.13	Ingress only
2021 Dec 5	884	1 m TNT	V	30	351	4.73	0.11	Full
		2.4 m TNT	u'	12.78	1243	4.89	0.62	Full
2021 Dec 20	888	2.4 m TNT	g'	12.78	1080	4.10	0.11	Full
2022 Jan 30	899	2.4 m TNT	z'	9.12	1353	3.81	0.14	Full
2022 Dec 16	985	2.4 m TNT	u'	12.78	765	3.20	0.53	Full
2023 Aug 19	1051	0.7 m TRT-SRO	R	30	288	2.98	0.25	Egress only
2023 Sep 29	1062	0.7 m TRT-SRO	R	30	373	3.82	0.27	Full
2023 Dec 1	1079	2.4 m TNT	g'	7.19	1230	2.62	0.10	Ingress only
2023 Dec 5	1080	0.7 m TRT-SRO	R	30	341	3.53	0.19	Full
2024 Jan 11	1090	2.4 m TNT	r'	1.7	5288	2.63	0.10	Full
2024 Aug 14	1148	0.7 m TRT-SRO	R	30	268	2.91	0.22	Ingress only
2024 Sep 24	1159	0.7 m TRT-SRO	V	30	344	4.72	0.20	Ingress only
2024 Oct 20	1166	0.7 m TRT-SRO	I	30	314	3.15	0.21	Full
2024 Dec 4	1178	0.7 m TRT-SRO	V	30	364	3.57	0.19	Full
2024 Dec 11	1180	1 m TNT	I	5	927	3.09	0.11	Egress only
		2.4 m TNT	z'	4.21	3847	4.53	0.16	Full

Notes.
[a] Epoch = 0 is the transit on 2012 December 2.
[b] PNR is the photometric noise rate (B. J. Fulton et al. 2011).

Table 3
The Initial Parameter Settings and Priors for Modeling Planetary Parameters with `TransitFit` for Both Ground-based and `TESS` Data

Parameter	Priors	Prior Distribution
P [days]	3.722479 ± 10^{-6}	A Gaussian distribution
T_0 [BJD]	2456263.57 ± 0.002	A Gaussian distribution
i [deg]	(86, 90)	Uniform distribution
a/R_*	(11, 14)	Uniform distribution
R_p/R_*[a]	(0.11, 0.15)	Uniform distribution
e	0	Fixed

Notes. The priors of P, T_0, i and a/R_* are set as the values in G. Á. Bakos et al. (2009).
[a] The same prior was used for R_p/R_* for each filter.

ephemeris was determined using the following relation:

$$t(E) = t_{0,l} + P_{\mathrm{orb},l} \times E, \quad (1)$$

where $t(E)$ is the calculated midtransit time at a given epoch E. The terms $t_{0,l}$ and $P_{\mathrm{orb},l}$ represent the reference midtransit time and the orbital period of the linear ephemeris model, respectively. Here, E denotes the epoch number, with $E = 0$ defined as the transit event occurring on 2012 December 2 (E. S. Ivshina & J. N. Winn 2022).

The best-fitting parameters were determined using the `emcee` Markov Chain Monte Carlo (MCMC) package (D. Foreman-Mackey et al. 2013), employing 50 walkers and 10^5 steps. To ensure convergence, a burn-in period of 10^4 steps was discarded for each walker. The sampling efficiency and convergence were assessed using the mean acceptance fraction (a_f), the integrated autocorrelation time (τ), and the effective number of independent samples (N_{eff}), all of which are summarized in Table 6.

From this linear ephemeris fit, the updated linear ephemeris was derived as

$$t(E) = 2456263.56879^{+0.00025}_{-0.00025} + 3.7224796^{+3\times10^{-7}}_{-3\times10^{-7}} \quad E. \quad (2)$$

The reduced chi-squared was calculated as $\chi^2_\nu = 11.6$ with 48 degrees of freedom. The Bayesian Information Criterion

Table 4
The Best-fit Planetary Parameters of WASP-11 b/HAT-P-10 b from `TransitFit` Compared with Literature Values

References	P (days)	i (deg)	a/R_*
G. Á. Bakos et al. (2009)	$3.7224747 \pm 6.5 \times 10^{-6}$	$88.6^{+0.5}_{-0.4}$	$11.93^{+0.2}_{-0.6}$
R. G. West et al. (2009)	$3.722465^{+6\times10^{-6}}_{-8\times10^{-6}}$	$89.8^{+0.2}_{-0.8}$	...
X.-b. Wang et al. (2014)	$3.7224767 \pm 1.81 \times 10^{-6}$	$89.14^{+0.50}_{-0.47}$	12.27 ± 0.24[a]
A. Kokori et al. (2023)	$3.7224792 \pm 1.8 \times 10^{-7}$	89.1 ± 0.5	12.30 ± 0.11
This study			
Ground based	$3.7224798 \pm 7 \times 10^{-8}$	88.2 ± 0.1	12.12 ± 0.04
TESS	$3.7224790 \pm 2 \times 10^{-7}$	89.7 ± 0.3	12.32 ± 0.07
Weighted mean values	$3.7224797 \pm 7 \times 10^{-8}$	88.28 ± 0.06	12.17 ± 0.04

Note.
[a] Reported as 0.0447 ± 0.0002 au.

(BIC) was determined to be $\mathrm{BIC} = \chi^2 + k \ln n = 565$, where k is the number of free parameters and n is the number of data points. The best-fit values for each parameter were derived from the marginalized posterior distributions shown in the corner plot. We report the median of the posterior samples as the central value, with the uncertainties corresponding to the 68% (1σ) interval, calculated from the 16th and 84th percentiles. Using the new linear ephemeris from Equation (2), we constructed the $O - C$ diagram for WASP-11 b/HAT-P-10 b, which displays the timing residuals between the observed midtransit times and the linear model, as presented in Figure 4.

4.2. Searching for Evidence of Orbital Decay

The study of close-in planets ($a < 0.1$ au), particularly hot Jupiters, is essential for investigating orbital decay, which provides a means to constrain the modified stellar tidal quality factor ($Q'_\star$). This phenomenon offers critical insights into the dynamical evolution of planetary systems, most notably through tidal orbital decay, mass loss, and apsidal precession. Measuring the rate of orbital decay in these systems is fundamental for characterizing stellar tidal dissipation and determining the remaining lifetimes of short-period planets (G. Maciejewski et al. 2016, 2021; K. C. Patra et al. 2017; V. K. Mannaday et al. 2020; S. W. Yee et al. 2020).

Following the study of orbital period variations in WASP-11 b/HAT-P-10 b by W. Wang et al. (2024), which reported an increasing orbital period in their LOOCV analysis, we examined our midtransit times to investigate potential orbital period variations and search for signs of orbital decay in WASP-11 b/HAT-P-10 b using the following equation:

$$t(E) = t_{0,d} + E \times P_{\mathrm{orb},d} + \frac{1}{2}\frac{dP_d}{dE}E^2, \tag{3}$$

where $t_{0,d}$ is a reference time of the orbital decay model. $P_{\mathrm{orb},d}$ is orbital period of the orbital decay model and dP_d/dE is the change of orbital in each orbit.

We also performed the fitting using MCMC in the same manner as the linear model. The corner plots displaying the posterior distributions of the best-fit parameters for both models are presented in Figure D1, and the results are summarized in Table 6. For the orbital decay model, we derived an orbital decay rate of $dP_d/dE = -6^{+9}_{-9} \times 10^{-10}$ days/orbit, with a reduced chi-squared of $\chi^2_\nu = 11.1$ (47 degrees of freedom) and a BIC of 533. Using the best-fit parameters from the orbital decay model, the timing residuals as a function of epoch E (calculated by subtracting the best-fit constant-period model) are shown in Figure 4. A comparison of the χ^2_ν values between the linear ephemeris and orbital decay models reveals no significant differences. We therefore conclude that there is no clear evidence of orbital decay in the WASP-11/HAT-P-10 system. The derived orbital decay rate exhibits a negative trend, which is consistent with the findings of S. Yalçınkaya et al. (2024) but contrasts with the increasing orbital period reported by W. Wang et al. (2024).

In addition to the orbital decay rate obtained from our analysis, we calculated the stellar tidal quality factor, $Q'_\star$, defined as (P. Goldreich & S. Soter 1966):

$$Q'_\star = -\frac{27}{2}\pi\left(\frac{M_p}{M_\star}\right)\left(\frac{a}{R_\star}\right)^{-5}\left(\frac{dP_d}{dE}\right)^{-1}P, \tag{4}$$

where M_p and $M_\star$ are the masses of the planet and host star, respectively, and $a/R_* = 12.17 \pm 0.04$ from our fitting results. The planetary and stellar masses were adopted from G. Á. Bakos et al. (2009). Using our derived orbital decay rate, we estimate $Q'_* \sim 5.1 \times 10^2$, which is significantly lower than theoretical predictions, in the range $10^5 \leqslant Q\star \leqslant 10^7$ (K. Penev et al. 2018). For comparison, S. Yalçınkaya et al. (2024) reported no significant periodic changes in the TTV diagram and derived an orbital decay rate of $dP/dE = -9.6 \pm 5.98 \times 10^{-10}$ day cycle^{-1}, corresponding to a stellar tidal quality factor of $Q'_* > 4.1 \times 10^2$. Our result is consistent with their lower limit and also indicates that any orbital decay is negligible and not detectable within current observational uncertainties.

4.3. Analysis of the Apsidal Precession Model

In addition to the linear and orbital decay analyses, the 50 midtransit times were investigated using an apsidal precession model. This model accounts for potential inverted parabolic trends by assuming a nonzero eccentricity, e, and an argument of periastron, ω, that precesses uniformly over time. Following A. Giménez & M. Bastero (1995), the midtransit times are

Table 5
The Planet-to-star Radius (R_p/R_*) and Limb-darkening Coefficients (LDCs) of WASP-11 b/HAT-P-10 b Derived with `TransitFit` Using the Coupled LDCs Fitting Mode

Filter	Midwavelength (μm)	Bandwidth (μm)	R_p/R_*	u_0	u_1
u' band	0.353	0.095	0.1369 ± 0.0003	0.503 ± 0.002	0.467 ± 0.002
g' band	0.467	0.172	0.1363 ± 0.0001	0.425 ± 0.001	0.435 ± 0.001
r' band	0.621	0.155	0.1342 ± 0.0001	0.326 ± 0.002	0.381 ± 0.002
i' band	0.754	0.168	0.1298 ± 0.0002	0.321 ± 0.002	0.387 ± 0.002
z' band	0.94	0.285	0.1331 ± 0.0002	0.322 ± 0.002	0.385 ± 0.002
V band	0.6	0.24	0.1350 ± 0.0003	0.325 ± 0.002	0.382 ± 0.002
I band	0.805	0.19	0.1281 ± 0.0003	0.325 ± 0.002	0.382 ± 0.002
R band	0.672	0.245	0.1331 ± 0.0001	0.325 ± 0.002	0.382 ± 0.002
TESS band	0.849	0.535	0.1271 ± 0.0002	0.501 ± 0.001	0.466 ± 0.002
Clear band	0.6	0.6	0.1284 ± 0.0002	0.424 ± 0.001	0.434 ± 0.001

expressed as:

$$t(E) = t_{0,a} + E \times P_s - \frac{eP_a}{\pi}\cos\omega(E), \quad (5)$$

where

$$\omega(E) = \omega_0 + \frac{d\omega}{dE}E, \quad (6)$$

$$P_s = P_a\left(1 - \frac{1}{2\pi}\frac{d\omega}{dE}\right). \quad (7)$$

In these equations, $t_{0,a}$ represents the reference midtransit time, e is the orbital eccentricity, P_a is the anomalistic period, ω_0 is the argument of periastron at $E = 0$, P_s is the sidereal period, and $d\omega/dE$ is the precession rate of the periastron.

The model parameters were estimated using the same MCMC configuration as the previous models. The best-fit parameters derived from the posterior distributions (Figure D1) indicate a nearly circular orbit with $e = 0.0003 \pm 0.0002$. The argument of periastron was found to be $\omega_0 = 3^{+2}_{-1}$ rad, with a precession rate of $d\omega/dE = 0.014 \pm 0.002$ rad/orbit. This model yielded $\chi^2_\nu = 11.4$ with 45 degrees of freedom and a BIC of 531. Despite the high precession rate resulting in the sinusoidal trend shown in Figure 4, the χ^2_ν values remain consistent with those of the linear and orbital decay models, showing no statistically significant improvement.

Comparing the BIC values among the three models, the apsidal precession model yielded the lowest BIC of 531, followed by the orbital decay model with a BIC of 533, and the linear model with a BIC of 565. The difference between the apsidal and decay models is statistically small with a ΔBIC of 2, providing no decisive evidence for one over the other. However, our analysis shows that the orbital decay rate lacks statistical significance, and the derived tidal quality factor for the host star is three orders of magnitude smaller than theoretical predictions. Given these discrepancies and the lack of strong statistical support, the orbital decay model can be ruled out based on the present timing data.

4.4. Line-of-sight Acceleration

Furthermore, orbital decay can be investigated by measuring line-of-sight acceleration, a phenomenon known as the Rømer effect. This effect shows that if the center of mass of the star-planet system accelerates along the line of sight with a magnitude of $\dot{\nu}_{\rm RV}$, the observed orbital period would change (L. G. Bouma et al. 2020; S. W. Yee et al. 2020; G. Maciejewski et al. 2021; V. K. Mannaday et al. 2022). Based on this phenomenon, an acceleration toward the observer causes the period to decrease, while an acceleration away from the observer causes the period to increase. Following the formula from G. Maciejewski et al. (2021), the relationship between the period change and the acceleration is given by:

$$\dot{\nu}_{RV} = \frac{\dot{P}_q}{P_q}c \quad (8)$$

where P_q represents the orbital period from the orbital decay model ($P_{\rm orb,d}$ in Table6), $\dot{P}_q$ is the period derivative, and c is the speed of light. By applying the formula $\dot{P}_q = \frac{1}{P_q}\frac{dP_q}{dE}$, we found that $\dot{P}_q = -5.5^{+7.6}_{-7.6}$ ms yr^{-1}. From Equation (8), the radial velocity acceleration ($\dot{\nu}_{\rm RV}$) is derived to be -0.014 ± 0.019m s^{-1} day^{-1}. To confirm this value, we calculated the linear acceleration from RV observations ($\dot{\gamma} = \dot{\nu}_{\rm RV}$) by using the `RadVel` Python package to fit the radial velocity curves (B. J. Fulton et al. 2018). We utilized the RV data from R. G. West et al. (2009). To perform the RV fitting, the orbit was assumed to be circular ($e = 0$). The orbital period and midtransit time were constrained using Gaussian priors from the values in Table 3. The argument of periastron (ω) was fixed to zero, while the RV semi-amplitude (K), the center-of-mass velocity (γ), the linear RV trend ($\dot{\gamma}$), the quadratic RV trend ($\ddot{\gamma}$) and the "jitter" radial velocity were allowed to vary. From the fitting, we obtained $K = 82.04 \pm 1.08$ m s^{-1} and $\gamma = 4.914 \pm 0.008$ km s^{-1}, which are consistent with the results reported by R. G. West et al. (2009). However, the fitted linear RV trend yields a positive value of $\dot{\gamma} = (1 \pm 50) \times 10^{-5}$ m s^{-1} day^{-1}. This discrepancy value differs by approximately three orders of magnitude from the estimate derived from Equation (8). Furthermore, the large uncertainties in both methods, based on the timing data ($\dot{\nu}_{\rm RV}$) and the RV fitting ($\dot{\gamma}$), make it difficult to draw clear conclusions about this phenomenon. Therefore, a longer observational baseline from both transit timing and radial velocity data is needed to confirm this effect in the system.

4.5. The Analysis of TTVs Periodicity

The search for unseen planetary companions using Lomb–Scargle periodogram analysis (N. R. Lomb 1976) was initially conducted for this system by L. Mancini et al. (2015) and later

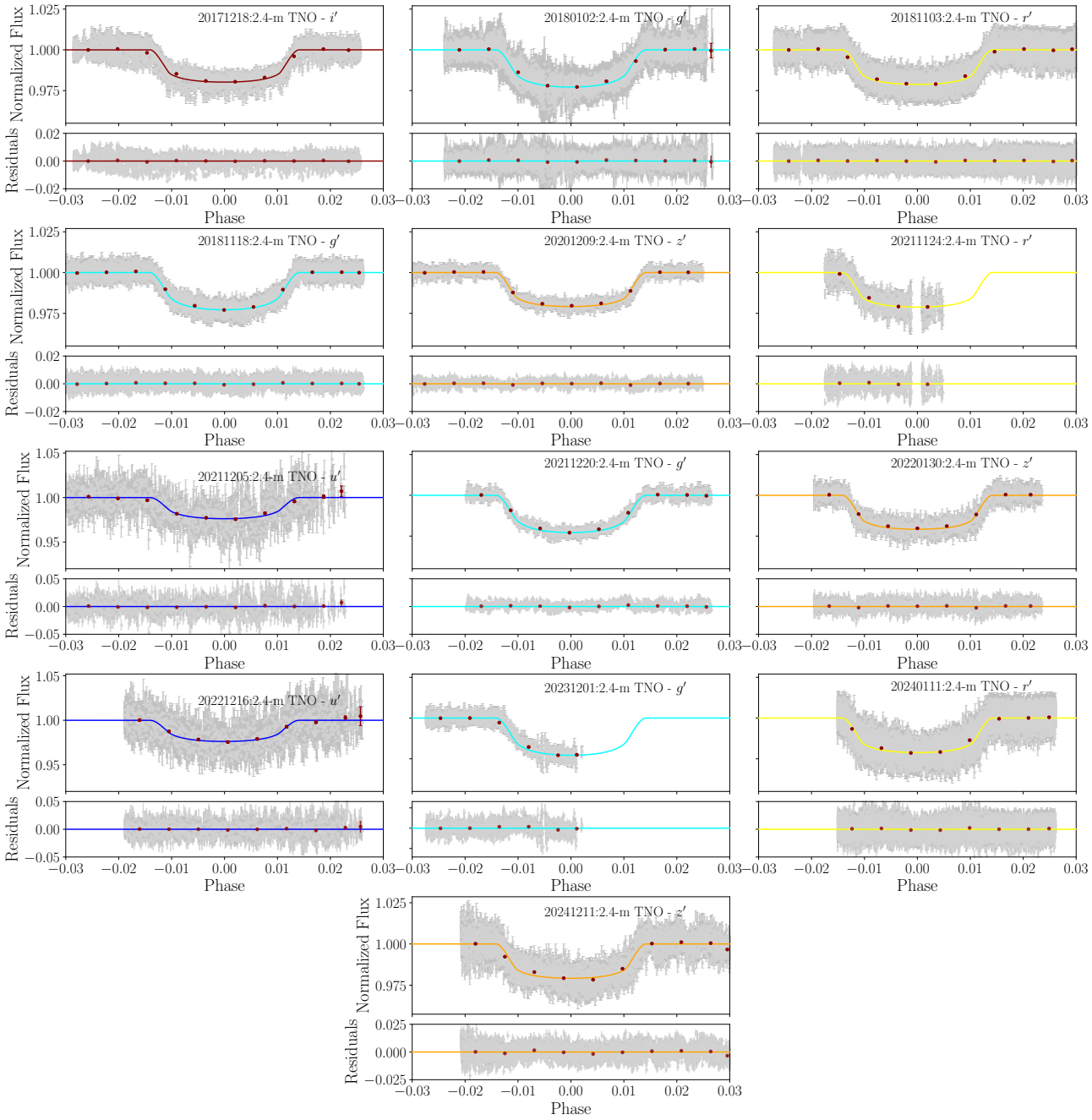

Figure 2. The normalized transit light curves of WASP-11 b/HAT-P-10 b observed with the 2.4 m telescope of the SPEARNET network (gray dots, upper panel). The best-fit model from `TransitFit` is shown as a solid line, and the residuals after model subtraction are displayed in the lower panel.

extended in studies by G. Maciejewski et al. (2023) and H. Er et al. (2024). In the present study, we investigated whether variations in the orbital period could be caused by additional planets influencing the system. The timing residuals ($O - C$) from Table B1 were used to search for periodic TTV signals. These signals were analyzed using the Generalized Lomb–Scargle periodogram (GLS; M. Zechmeister & M. Kürster 2009). The false-alarm probability (FAP) for the highest-power peaks was determined using the analytical probability method described by M. Zechmeister & M. Kürster (2009), as implemented in the `PyAstronomy` package (S. Czesla et al. 2019).[15]

The GLS results are shown in Figure 5. The periodogram shows the highest-power peak at 0.24, corresponding to a frequency of 0.3164 ± 0.0002 cycles period^{-1} and a FAP of 73%. Based on this analysis, no statistically significant TTV signal is detected that would indicate the presence of an additional planet in the WASP-11/HAT-P-10 system.

5. Atmospheric Modeling in Optical Wavelength

Using transmission spectroscopy, the atmospheric composition of a planet can be investigated in detail (S. Seager & D. D. Sasselov 2000). For hot Jupiters, numerous studies have explored the presence of atomic and molecular species such as Na, K, and TiO/VO, as well as the effects of clouds, hazes, and Rayleigh scattering in the optical wavelength range

[15] PyAstronomy: https://github.com/sczesla/PyAstronomy.

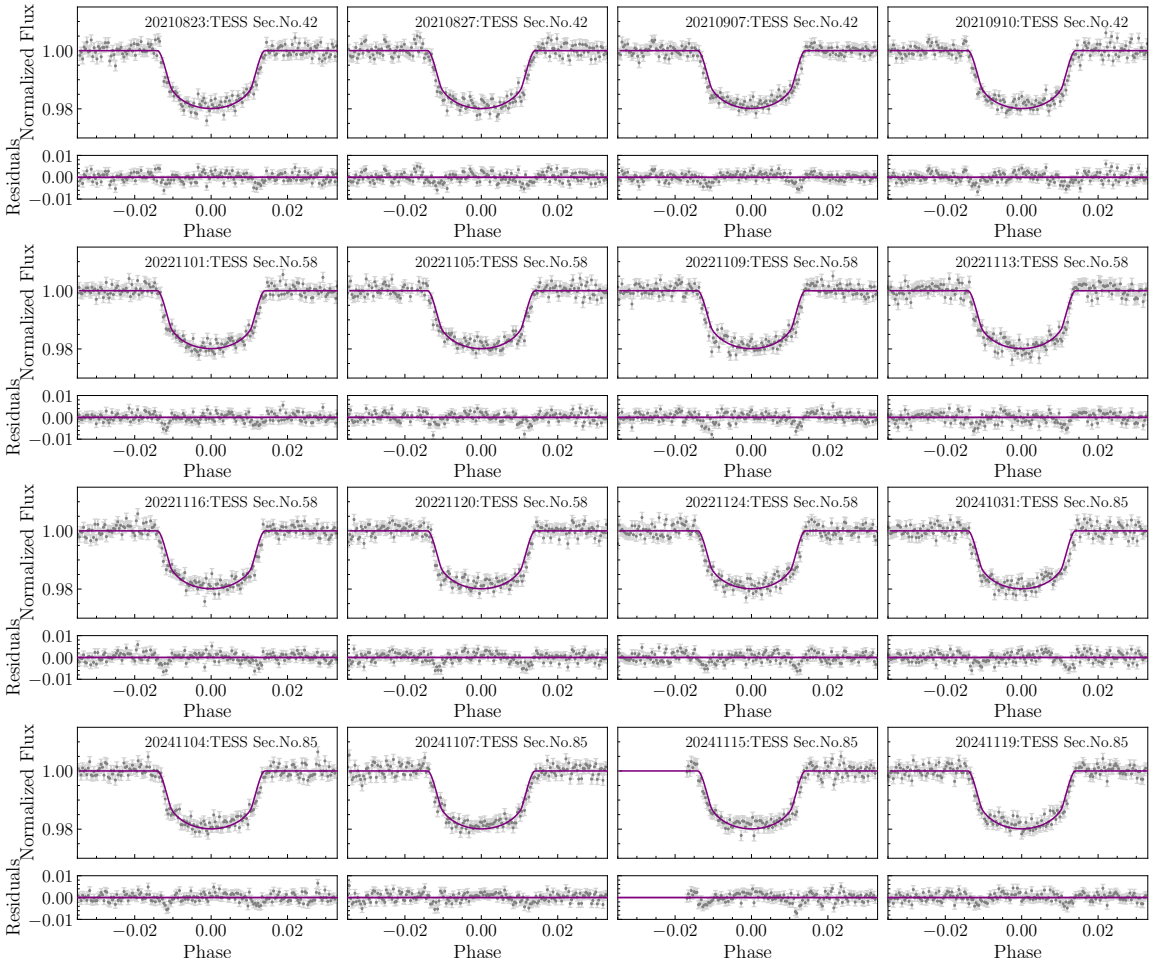

Figure 3. The normalized transit light curves of WASP-11 b/HAT-P-10 b observed by TESS (gray dots, upper panel), with the best-fit model from TransitFit shown as solid lines. The residuals after model subtraction are displayed in the lower panel.

(D. K. Sing et al. 2016; P. Spyratos et al. 2023; C. Fairman et al. 2024). Considering the R_p/R_* values derived from different filter bands with TransitFit (listed in Table 5, Section 3), we find that the planetary radius appears larger in the blue band, which may be indicative of Rayleigh scattering (A. Lecavelier Des Etangs et al. 2008; J. Kirk et al. 2017).

We performed the atmospheric retrieval analysis using the open-source code PLanetary Atmospheric Transmission for Observer Noobs (PLATON[16] M. Zhang et al. 2019). PLATON provides a fast framework for forward modeling and retrieval of exoplanet atmospheres. It employs PyMultiNest, a nested sampling algorithm, to compute the Bayesian evidence ($\mathcal{Z}$) and posterior distributions for the retrieval analysis (F. Feroz et al. 2009). For this study, the planet-to-star radius ratios (R_p/R_*) listed in Table 5, covering wavelengths from 0.3 to 0.9 μm across all filters except the *clear* filter, were used for atmospheric retrieval.

During the retrieval, the forward optical transmission spectrum was modeled assuming an isothermal atmosphere in chemical equilibrium, with the cloud-top pressure set to 10^5 Pa. The host star radius was adopted from G. Á. Bakos et al. (2009). We retrieved the planetary temperature (T), the metallicity ($\log Z$), and the carbon-to-oxygen ratio (C/O), which determines the relative molecular abundances. To account for clouds and hazes, we included a scattering factor and a scattering slope. An error multiplier was incorporated to scale the observational uncertainties. To ensure a robust exploration of the parameter space, the fitting was performed with 1000 live points and a termination criterion of $\Delta \ln Z < 0.1$ using the nested sampling method. This process generated posterior distributions for each parameter, with the resulting corner plots displaying the median values and the associated 1σ intervals based on the 16th and 84th percentiles. The priors and the retrieved results are summarized in Table 7.

The atmospheric retrieval indicates that WASP-11 b/HAT-P-10 b has an isothermal temperature of approximately 1000 K. At a cloud-top pressure of 10^5 Pa, the planetary radius is 0.99 ± 0.02 $R_{\rm Jup}$, with a corresponding mass of 0.49 ± 0.01 $M_{\rm Jup}$. The host star radius was found to be 0.79 ± 0.01 $R_\odot$. These results are summarized in Table 7 and Figure 6, with the posterior distributions of the model parameters presented in Figure E1. A strong Rayleigh scattering slope is observed from blue optical to near-infrared wavelengths, characterized by a scattering factor of $\log f_{\rm scat} = 3 \pm 1$ and a C/O ratio of 1.1 ± 0.6. Due to the large uncertainty in the C/O ratio, the molecular composition of the atmosphere cannot be robustly constrained. Consequently, additional near-infrared observations are necessary to better characterize the atmospheric constituents of WASP-11 b/HAT-P-10 b.

The strong Rayleigh scattering observed in the atmosphere of WASP-11 b/HAT-P-10 b is similar to that detected in other planetary systems, such as WASP-6 b (N. Nikolov et al. 2015;

[16] PLATON: https://github.com/ideasrule/platon.

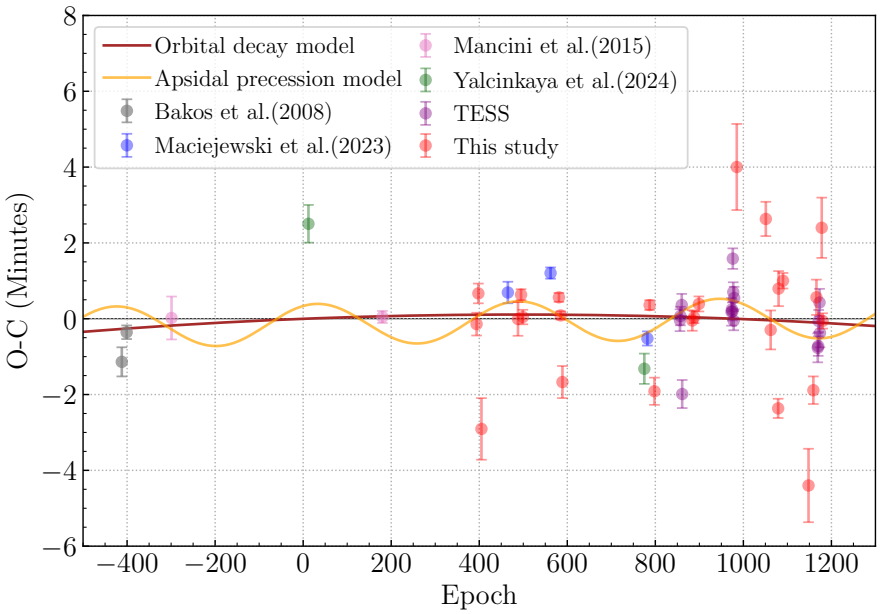

Figure 4. The $O - C$ diagram and best-fit model for WASP-11 b/HAT-P-10 b, showing data from G. Á. Bakos et al. (2009; gray dots), L. Mancini et al. (2015; pink dots), G. Maciejewski et al. (2023; blue dots), S. Yalçınkaya et al. (2024; green dots), TESS (purple dots), and this study (red dots). Timing residuals for the orbital decay and apsidal precession models are shown as brown and orange curves, respectively.

Table 6
The Uniform Priors and Best-fit Parameters from MCMC Transit-timing Analyses

Parameter	Uniform Distribution Priors	Best-fit Values
Constant-period model		
$P_{\mathrm{orb},l}$ [days]	(3.72246, 3.72249)	$3.7224796^{+3\times10^{-7}}_{-3\times10^{-7}}$
$t_{0,l}$ [$\mathrm{BJD_{TDB}}$ + 2450000]	(6263.567, 6263.574)	$6263.56879^{+0.0003}_{-0.0003}$
χ^2_{red}	11.6	
BIC	565	
a_f	0.6	
τ	40	
N_{eff}	122,606	
Orbital decay model		
$P_{\mathrm{orb},d}$ [days]	(3.72246, 3.72249)	$3.7224799^{+6\times10^{-7}}_{-6\times10^{-7}}$
$t_{0,d}$ [$\mathrm{BJD_{TDB}}$ + 2450000]	(6263.567, 6263.574)	$6263.56879^{+0.0002}_{-0.0002}$
dP_{d}/dE [days/orbit]	(−0.5, 0.5)	$-6^{+9}_{-9} \times 10^{-10}$
χ^2_{red}	11.1	
BIC	533	
a_f	0.6	
τ	49	
N_{eff}	101,544	
Apsidal precession model		
P_s [days]	(3.72246, 3.72249)	$3.7224797^{+3\times10^{-7}}_{-3\times10^{-7}}$
$t_{0,a}$ [$\mathrm{BJD_{TDB}}$ + 2450000]	(6263.567, 6263.574)	$6263.56869^{+0.0003}_{-0.0003}$
e	(0, 0.002)	$0.0003^{+0.0002}_{-0.0002}$
ω_0 [rad]	(0, 2π)	3^{+2}_{-1}
$d\omega/dE$ [rad/orbit]	(0, 0.02)	$0.014^{+0.002}_{-0.002}$
χ^2_{red}	11.4	
BIC	531	
a_f	0.4	
τ	1506	
N_{eff}	3320	

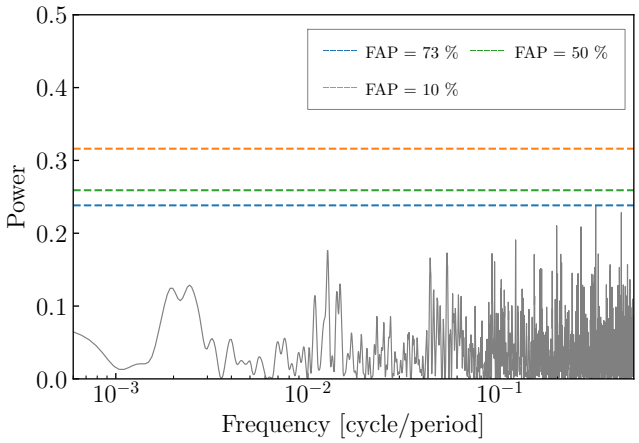

Figure 5. The GLS periodogram of the timing residuals from 50 midtransit times derived with TransitFit. The false-alarm probability (FAP) levels are indicated by dashed lines.

A. L. Carter et al. 2020; F. Grübel et al. 2025) and HAT-P-12b (D. K. Sing et al. 2016; I. Wong et al. 2020), where high-altitude Rayleigh-scattering clouds contribute to the effect. Since the host star of WASP-11 b/HAT-P-10 b is a K-type star in a binary system, the observed scattering signature could potentially be influenced by stellar activity or contamination from the companion star, as discussed by C. Jiang et al. (2021). However, no clear signs of stellar activity are evident in the TESS light curves. Therefore, long-term monitoring of the transmission spectrum at higher spectral resolution is required to confirm the presence and origin of the strong Rayleigh scattering in this system.

6. Summary and Conclusions

We present a new set of 31 optical transit light curves of the hot Jupiter WASP-11 b/HAT-P-10 b obtained with the ground-

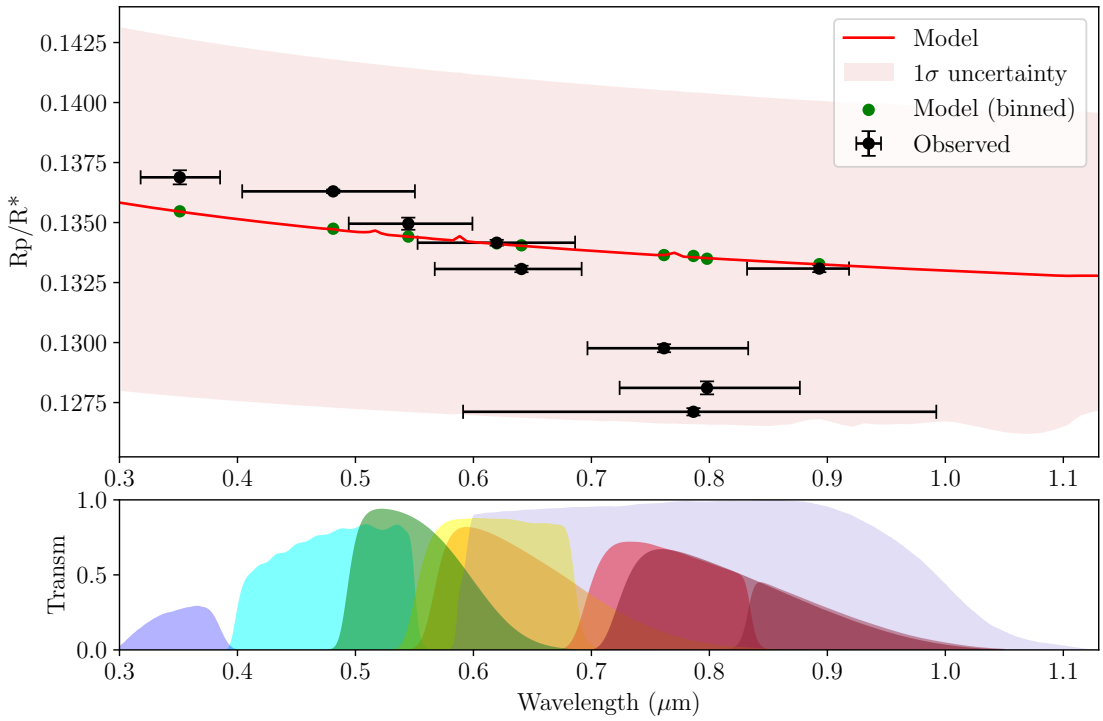

Figure 6. Top panel: retrieved transmission spectrum of WASP-11 b/HAT-P-10 b with forward models generated using PLATON. Bottom panel: Band-pass filter profiles for u', g', V, r', R, i', I, *TESS*, and z' (from left to right).

Table 7
Prior Ranges, Distribution Types, and the Resulting Best-fit Parameters Obtained from the PLATON Atmospheric Retrieval for WASP-11 b/HAT-P-10 b

Parameter	Prior Range	Prior Distribution	Retrieved Values
R_s $[R_\odot]$	0.79 ± 0.01	Gaussian	$0.79^{+0.01}_{-0.01}$
M_p $[M_{\rm jup}]$	0.487 ± 0.01	Gaussian	$0.49^{+0.01}_{-0.01}$
R_p $[R_{\rm jup}]$	(0.804, 1.206)	Uniform	$0.99^{+0.02}_{-0.02}$
T $[K]$	(450, 1350)	Uniform	1000^{+200}_{-300}
$\log_{Z/Z_\odot}$	(−0.5, 2.0)	Uniform	$0.5^{+0.8}_{-0.7}$
$\log_{\rm ScatteringFactor}$	(0, 5)	Uniform	3^{+1}_{-1}
C/O ratio	(0.1, 2.0)	Uniform	$1.1^{+0.6}_{-0.6}$
Error multiple	(0.5, 20)	Uniform	18^{+2}_{-2}

Note. The retrieved values represent the medians of the posterior distributions, with uncertainties corresponding to the 1σ intervals.
The priors of R_s, M_p and R_p are set as the values from G. Á. Bakos et al. (2009).

based SPEARNET telescope network. This new dataset was combined with previously published ground-based light curves and TESS data. All light curves were modeled using TransitFit. From the fitting, WASP-11 b/HAT-P-10 b exhibits an orbital period of $3.7224797 \pm 7 \times 10^{-8}$ days, an inclination of $i = 88.^{\circ}28 \pm 0.^{\circ}06$, and a star–planet separation of $a/R_* = 12.17 \pm 0.04$, all consistent with previous studies.

Midtransit times from a total of 50 epochs, derived using TransitFit, were used to update the linear ephemeris and to search for evidence of orbital decay and apsidal precession. The updated linear ephemeris is $t(E) = 2456263.56879 \pm 0.00025 + (3.7224796 \pm 3 \times 10^{-7}) \times E$. While the model comparisons show similar reduced chi-squared and BIC values, the derived tidal quality factor is three orders of magnitude smaller than theoretical expectations. The orbital decay scenario is physically inconsistent and is ruled out for the current timing data. Additionally, the line-of-sight acceleration analysis finds a discrepancy between the acceleration values derived from TTV and RV data. Therefore, this study and the current data do not support the presence of this phenomenon. We also searched for TTV signals from potential unseen planetary companions using periodogram analysis. However, no significant TTV signals were detected due to the high false-alarm probability, indicating the absence of additional planets within detectable limits. We acknowledge that the reduced chi-squared values for both the linear and orbital decay models are relatively high. We attribute this primarily to the sensitivity of high-precision observations to low-level astrophysical noise, such as stellar activity, starspot crossings, or granulation. These physical phenomena introduce small fluctuations in midtransit times. Furthermore, the residuals likely contain low-amplitude dynamical variations or remaining differences between datasets that are not fully captured by simple orbital models. Since our periodogram analysis did not identify a definitive periodic signal, we conclude that the linear model remains the best choice. The high-reduced chi-squared reflects the difficulty of combining data from multiple telescopes when stellar and dynamical noise are present over a long period.

For atmospheric characterization, the planet-to-star radius ratios (R_p/R_*) from nine filters, spanning optical to near-infrared wavelengths, were used in transmission spectroscopy analysis with PLATON. The results reveal a strong Rayleigh scattering slope from the blue optical to near-infrared, with a C/O ratio of $1.1^{+0.6}_{-0.6}$. This strong Rayleigh scattering is similar to that seen in WASP-6b (N. Nikolov et al. 2015; A. L. Carter et al. 2020; F. Grübel et al. 2025) and HAT-P-12b (D. K. Sing et al. 2016; I. Wong et al. 2020). Although the host star is a K-type star in a binary system, no clear stellar activity is evident in the TESS light curves. Long-term, high-resolution

spectroscopic monitoring is therefore needed to confirm the presence and origin of the Rayleigh scattering, making WASP-11 b/HAT-P-10 b a promising target for future observations.

Acknowledgments

We thank the referee for their comments and suggestions, which have improved the quality of this work. This work is supported by the Fundamental Fund of Thailand Science Research and Innovation (TSRI) through the National Astronomical Research Institute of Thailand (Public Organization; FFB690072/0269). I.J. acknowledges support from the National Science and Technology Council (NSTC), Taiwan, under grants NSTC 113-2112-M-007-030 and NSTC 114-2112-M-007-029. This paper is based on observations made with ULTRASPEC at the Thai National Observatory, the Thai Robotic Telescopes, and the Regional Observatories for the Public under the operation of the National Astronomical Research Institute of Thailand (Public Organization). This work used the available data based on observations made with the TESS mission, obtained from the MAST data archive at the STScI (TESS Team 2021). Funding for the TESS mission is provided by the NASA Explorer Program. STScI is operated by the AURA, Inc., under NASA contract NAS 5–26555.

Facilities: TESS, 2.4-m (TNT), 1-m (TNT), TRT, 0.7-m (ROP-NM) and 0.7-m (ROP-CC).

Software: `sextractor` (E. Bertin & S. Arnouts 1996), `Astrometry.net` (D. Lang et al. 2010), `TransitFit` (J. J. C. Hayes et al. 2024), `PLATON` (M. Zhang et al. 2019).

Appendix A
WASP-11 b/HAT-P-10 b Transit Light Curves from SPEARNET

The transit light curves of WASP-11 b/HAT-P-10 b, obtained from SPEARNET ground-based multiband photometric observations, are provided in Table A1.

Table A1
The Normalized Transit Light Curves of WASP-11 b/HAT-P-10 b, Observed by the SPEARNET Telescope Network

Epoch	BJD	Normalized Flux	Normalized Flux Error
394	2457730.12572	1.009	0.005
	2457730.12798	0.990	0.006
	2457730.12947	1.002	0.007
	...		...
398	2457745.03460	1.004	0.004
	2457745.03500	0.999	0.004
	2457745.03539	1.000	0.004
	...		...
405	2457771.07131	0.995	0.004
	2457771.07174	0.998	0.004
	2457771.07217	0.999	0.004
	...		...
...	...	...	...

Note. The full Table is available in machine-readable form.

(This table is available in its entirety in machine-readable form in the online article.)

Appendix B
Midtransit Times and $O - C$ of WASP-11 b/HAT-P-10 b

The midtransit times derived with `TransitFit` and the timing residuals ($O - C$), calculated from Equation (2), are listed in Table B1.

Table B1
Midtransit Times (t_m) and Timing Residuals ($O - C$) for 50 Epochs of WASP-11 b/HAT-P-10 b

Epoch	$t_m + 2450000$ (BJD$_{\rm TDB}$)	$(O - C)$ (days)	References
−412	4729.90642 ± 0.00027	−0.00079	(a)
−401	4770.85432 ± 0.00012	−0.00025	(a)
−299	5150.54741 ± 0.00039	0.00001	(b)
...	...	...	...
...	...	...	...

Note. The full Table is available in machine-readable form. Data Source: (a) G. Á. Bakos et al. (2009) (b) L. Mancini et al. (2015) (c) S. Yalçınkaya et al. (2024), (d) This study, (e) G. Maciejewski et al. (2023) and (f) `TESS`.

(This table is available in its entirety in machine-readable form in the online article.)

Appendix C
Individual WASP-11 b/HAT-P-10 b Transit Light Curves from SPEARNET Observations

The individual transit light curves of WASP-11 b/HAT-P-10 b observed with the SPEARNET telescope network are shown in Figure C1. The plots include the best-fitting models and their corresponding residuals.

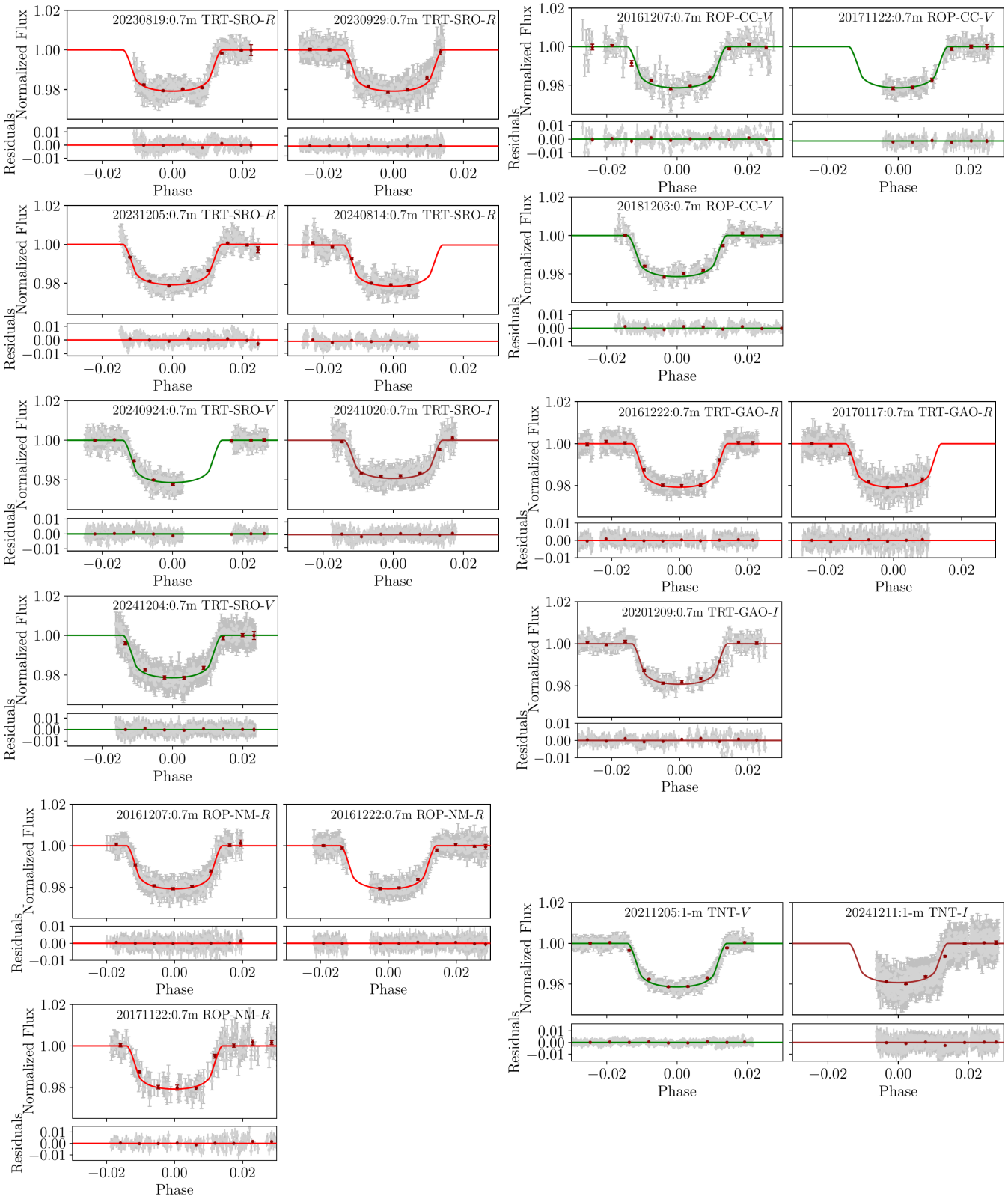

Figure C1. The normalized, individual transit light curves of WASP-11 b/HAT-P-10 b observed with the SPEARNET telescope network (gray dots, upper panel), including TRT-SRO, ROP-CC, TRT-GAO, ROP-NM, and the 1 m TNT. The best-fitting model from `TransitFit` is shown as a solid line. The corresponding residuals are displayed in the lower panel.

Appendix D
Posterior Probability Distribution of the MCMC Transit-timing Analyses

This section presents the corner plots illustrating the posterior probability distributions derived from the MCMC transit-timing analyses for the three models, as shown in Figure D1.

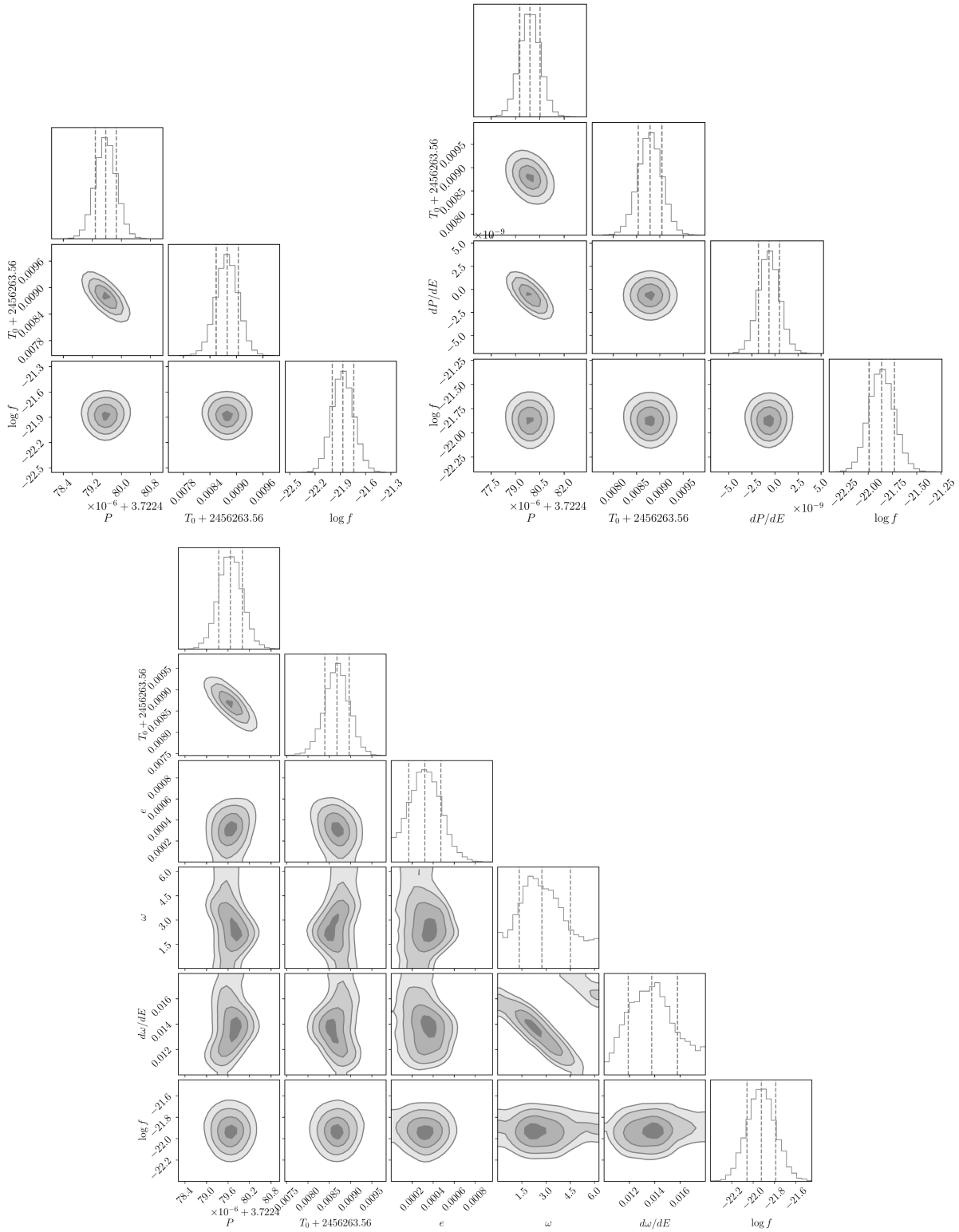

Figure D1. Posterior probability distribution of the MCMC fitting parameters for the constant-period, orbital decay and apsidal precession models, respectively.

Appendix E
Posterior Probability Distribution from Atmospheric Modeling with PLATON

In Figure E1, we present the retrieved posterior distributions of the atmospheric parameters for WASP-11 b/HAT-P-10 b. These were obtained using the PLATON code, which employs a nested sampling algorithm for the retrieval process.

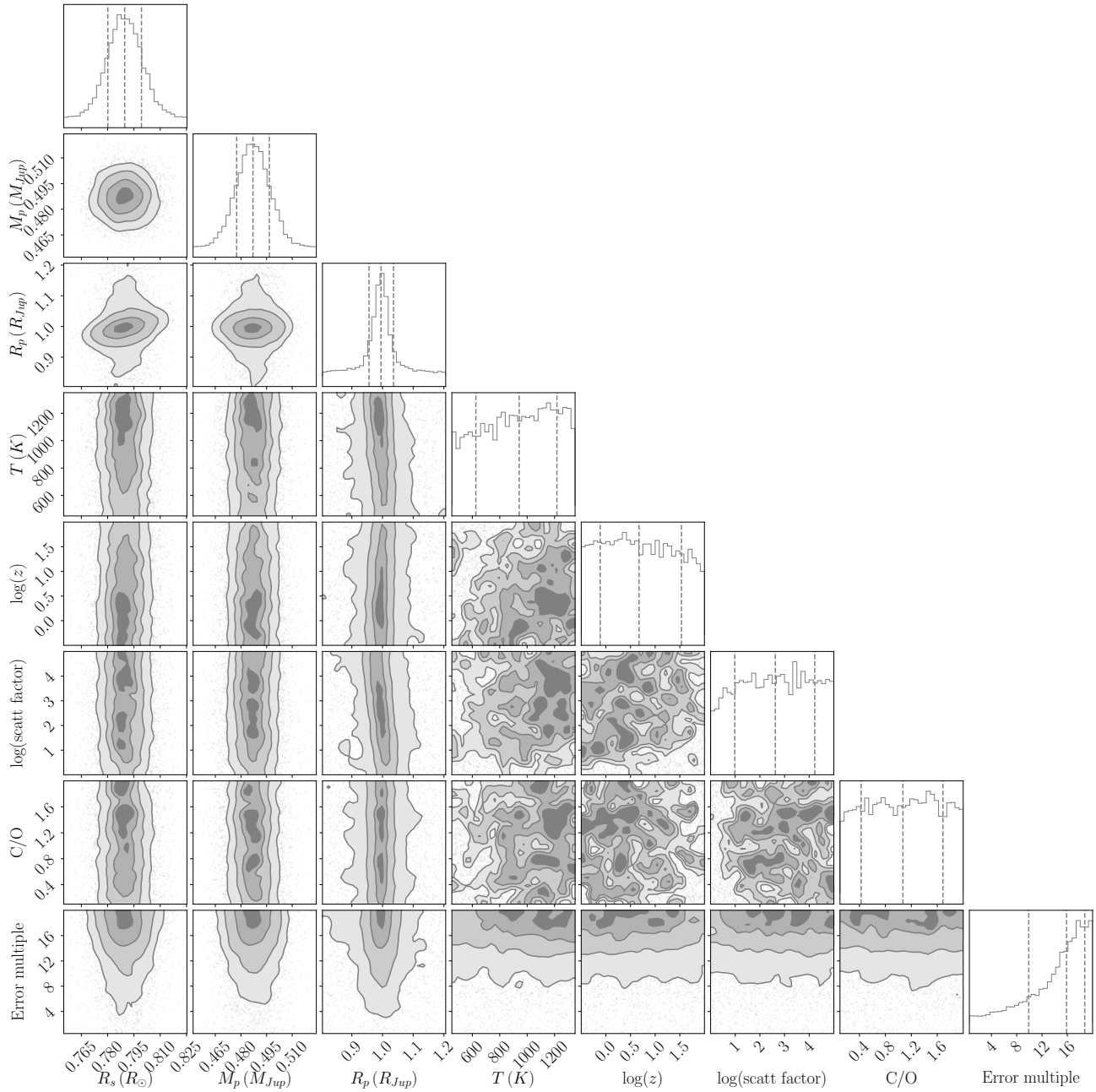

Figure E1. The posterior distributions for the atmospheric parameters of WASP-11 b/HAT-P-10 b retrieved using PLATON.

ORCID iDs

Napaporn A-thano https://orcid.org/0000-0001-7234-7167
Supachai Awiphan https://orcid.org/0000-0003-3251-3583
Eamonn Kerins https://orcid.org/0000-0002-1743-4468
Akshay Priyadarshi https://orcid.org/0000-0003-1143-0877
Iain McDonald https://orcid.org/0000-0003-0356-0655
Ing-Guey Jiang https://orcid.org/0000-0001-7359-3300
Yogesh C. Joshi https://orcid.org/0000-0001-8657-1573
Fan Yang https://orcid.org/0000-0002-6039-8212
Patcharawee Munsaket https://orcid.org/0009-0000-3885-4229
Yasir Abdul Qadir https://orcid.org/0000-0001-5162-4225
Vik S Dhillon https://orcid.org/0000-0003-4236-9642

References

A-thano, N., Awiphan, S., Jiang, I.-G., et al. 2023, AJ, 166, 223
Agol, E., Steffen, J., Sari, R., & Clarkson, W. 2005, MNRAS, 359, 567
Awiphan, S., Kerins, E., Pichadee, S., et al. 2016, MNRAS, 463, 2574
Bai, L., Gu, S., Wang, X., et al. 2022, MNRAS, 512, 3113
Bakos, G. Á., Pál, A., Torres, G., et al. 2009, ApJ, 696, 1950
Bertin, E., & Arnouts, S. 1996, A&AS, 117, 393
Bonomo, A. S., Desidera, S., Benatti, S., et al. 2017, A&A, 602, A107
Bouma, L. G., Winn, J. N., Howard, A. W., et al. 2020, ApJL, 893, L29
Carter, A. L., Nikolov, N., Sing, D. K., et al. 2020, MNRAS, 494, 5449
Czesla, S., Schröter, S., Schneider, C. P., et al. 2019, PyA: Python astronomy-related packages, Astrophysics Source Code Library, ascl:1906.010
Dhillon, V. S., Marsh, T. R., Atkinson, D. C., et al. 2014, MNRAS, 444, 4009
Edwards, B., Changeat, Q., Tsiaras, A., et al. 2023, AJ, 166, 158
Er, H., Karaman, N., Özdönmez, A., Nasiroglu, İ., & Gürbulak, B. B. 2024, NewA, 107, 102138
Fairman, C., Wakeford, H. R., & MacDonald, R. J. 2024, AJ, 167, 240
Feroz, F., Hobson, M. P., & Bridges, M. 2009, MNRAS, 398, 1601
Foreman-Mackey, D., Hogg, D. W., Lang, D., & Goodman, J. 2013, PASP, 125, 306
Fulton, B. J., Petigura, E. A., Blunt, S., & Sinukoff, E. 2018, PASP, 130, 044504
Fulton, B. J., Shporer, A., Winn, J. N., et al. 2011, AJ, 142, 84
Giménez, A., & Bastero, M. 1995, Ap&SS, 226, 99
Goldreich, P., & Soter, S. 1966, Icar, 5, 375
Grübel, F., Molaverdikhani, K., Ercolano, B., et al. 2025, MNRAS, 536, 324
Hayes, J. J. C., Priyadarshi, A., Kerins, E., et al. 2024, MNRAS, 527, 4936
Husser, T. O., Wende-von Berg, S., Dreizler, S., et al. 2013, A&A, 553, A6
Irwin, J. B. 1952, ApJ, 116, 211
Ivshina, E. S., & Winn, J. N. 2022, ApJS, 259, 62
Jenkins, J. M., Twicken, J. D., McCauliff, S., et al. 2016, SPIE, 9913, 99133E
Jiang, C., Chen, G., Pallé, E., et al. 2021, A&A, 656, A114
Kanodia, S., & Wright, J. 2018, RNAAS, 2, 4
Kirk, J., Wheatley, P. J., Louden, T., et al. 2017, MNRAS, 468, 3907
Knutson, H. A., Fulton, B. J., Montet, B. T., et al. 2014, ApJ, 785, 126
Kokori, A., Tsiaras, A., Edwards, B., et al. 2023, ApJS, 265, 4
Kreidberg, L. 2015, PASP, 127, 1161
Lang, D., Hogg, D. W., Mierle, K., Blanton, M., & Roweis, S. 2010, AJ, 139, 1782
Lecavelier Des Etangs, A., Pont, F., Vidal-Madjar, A., & Sing, D. 2008, A&A, 481, L83
Lomb, N. R. 1976, Ap&SS, 39, 447
Maciejewski, G., Dimitrov, D., Fernández, M., et al. 2016, A&A, 588, L6
Maciejewski, G., Fernández, M., Aceituno, F., et al. 2021, A&A, 656, A88
Maciejewski, G., Fernández, M., Sota, A., et al. 2023, AcA, 73, 57
Mancini, L., Esposito, M., Covino, E., et al. 2015, A&A, 579, A136
Mannaday, V. K., Thakur, P., Jiang, I.-G., et al. 2020, AJ, 160, 47
Mannaday, V. K., Thakur, P., Southworth, J., et al. 2022, AJ, 164, 198
Ngo, H., Knutson, H. A., Hinkley, S., et al. 2015, ApJ, 800, 138
Nikolov, N., Sing, D. K., Burrows, A. S., et al. 2015, MNRAS, 447, 463
Parviainen, H., & Aigrain, S. 2015, MNRAS, 453, 3821
Patra, K. C., Winn, J. N., Holman, M. J., et al. 2017, AJ, 154, 4
Penev, K., Bouma, L. G., Winn, J. N., & Hartman, J. D. 2018, AJ, 155, 165
Ricker, G. R., Winn, J. N., Vanderspek, R., et al. 2014, SPIE, 9143, 914320
Seager, S., & Sasselov, D. D. 2000, ApJ, 537, 916
Sing, D. K., Fortney, J. J., Nikolov, N., et al. 2016, Natur, 529, 59
Speagle, J. S. 2020, MNRAS, 493, 3132
Spyratos, P., Nikolov, N. K., Constantinou, S., et al. 2023, MNRAS, 521, 2163
TESS Team 2021, TESS Light Curves - All Sectors, STScI/MAST, doi:10.17909/T9-NMC8-F686
Tody, D. 1986, SPIE, 627, 733
Tody, D. 1993, ASPC, 52, 173
Wang, W., Zhang, Z., Chen, Z., et al. 2024, ApJS, 270, 14
Wang, X.-b., Gu, S.-h., Collier Cameron, A., et al. 2014, AJ, 147, 92
West, R. G., Collier Cameron, A., Hebb, L., et al. 2009, A&A, 502, 395
Wong, I., Benneke, B., Gao, P., et al. 2020, AJ, 159, 234
Yalçınkaya, S., Esmer, E. M., Baştürk, Ö., et al. 2024, MNRAS, 530, 2475
Yee, S. W., Winn, J. N., Knutson, H. A., et al. 2020, ApJL, 888, L5
Zechmeister, M., & Kürster, M. 2009, A&A, 496, 577
Zhang, M., Chachan, Y., Kempton, E. M. R., & Knutson, H. A. 2019, PASP, 131, 034501